

DIFFERENCES BETWEEN THE OPTICAL/ULTRAVIOLET SPECTRA OF X-RAY BRIGHT AND X-RAY FAINT QSOs

PAUL J. GREEN

Harvard-Smithsonian Center for Astrophysics, 60 Garden Street, Cambridge, MA 02138; pgreen@cfa.harvard.edu

Received 1997 July 29; accepted 1997 December 4

ABSTRACT

We contrast measurements of composite optical and ultraviolet (UV) spectra constructed from samples of QSOs defined by their soft X-ray brightness. X-ray bright (XB) composites show stronger emission lines in general, but particularly from the narrow-line region. The difference in the $[\text{O III}]/\text{H}\beta$ ratio is particularly striking, and is even more so when blended Fe II emission is properly subtracted. The correlation of this ratio with X-ray brightness was a principal component of QSO spectral diversity found by Boroson & Green. We find here that other, much weaker narrow optical forbidden lines ($[\text{O II}]$ and $[\text{Ne V}]$) are enhanced by factors of 2 to 3 in our XB composites, and that narrow line emission is also strongly enhanced in the XB UV composite. Broad permitted-line fluxes are slightly larger for all XB spectra, but the narrow-/broad-line ratio stays similar or increases strongly with X-ray brightness for all strong permitted lines except $\text{H}\beta$.

Spectral differences between samples divided by their relative X-ray brightness (as measured by α_{ox}) exceed those seen between complementary samples divided by luminosity or radio loudness. We propose that the Baldwin effect may be a secondary correlation to the primary relationship between α_{ox} and emission line equivalent width. We conclude that either (1) W_λ depends primarily on the *shape* of the ionizing continuum, as crudely characterized here by α_{ox} , or (2) both W_λ and α_{ox} are related to some third parameter characterizing the QSO physics. One such possibility is intrinsic warm absorption; a soft X-ray absorber situated between the broad and narrow line regions can successfully account for many of the properties observed.

Subject headings: galaxies: active — quasars: emission lines — quasars: general — ultraviolet: galaxies — X-rays: galaxies

1. INTRODUCTION

Most QSOs have been discovered by virtue of their strong optical/UV emission lines or nonstellar colors in this bandpass. Our understanding to date of the violent inner regions of active galactic nuclei (AGNe) also derive in large part from their optical/ultraviolet (OUV) spectra. The production of QSO emission lines is widely attributed to photoionization and heating of the emitting gas by the UV to X-ray continuum (see, e.g., Ferland & Shields 1985; Krolik & Kallman 1988). Studies investigating the relationship of emission lines to continuum radiation have a long history in the field, but several strong observational relationships remain unexplained.

If the proportionality between line and continuum strength were linear, then diagnostics such as line ratios and W_λ would be independent of continuum luminosity. Baldwin (1977) first noticed that, in high-redshift quasars, the W_λ of the C IV 1550 Å emission line in quasars decreases with increasing UV (1450 Å) luminosity. The Baldwin effect (BEff, hereafter) was also found to be strong for ions such as O VI, N V, He II, C III], Mg II, and Ly α (see, e.g., Tytler & Fan 1992; Zamorani et al. 1992). The initial excitement about the potential for the BEff as a standard candle and cosmological probe has faded; the dispersion in the relationship is too large. Neither the source of that dispersion nor the cause of the BEff itself have been definitively identified. However, some possible explanations for the BEff have been offered, one being a dependence of the continuum spectral energy distribution (SED) on luminosity (Zheng & Malkan 1993; Green 1996).

Many important lines respond primarily to the extreme ultraviolet (EUV) or soft X-ray continuum. Unfortunately,

the EUV band is severely obscured by Galactic absorption. However, constraints on the ionizing continuum are available through analysis of the adjacent UV and soft X-ray windows. In a small, uniform sample of optically selected QSOs (Laor et al. 1997), the strongest correlation found between X-ray continuum and optical emission line parameters was of the soft X-ray spectral slope α_x (where $f_\nu \propto \nu^{-\alpha_x}$) with the FWHM of the $\text{H}\beta$ emission line. Strong correlations between α_x , $L_{[\text{O III}]}$, Fe II/ $\text{H}\beta$, and the $[\text{O III}]/\text{H}\beta$ ratio were seen both there and in previous QSO studies (e.g., Boroson & Green 1992). The latter authors found that most of the variation in the observed properties of low-redshift QSOs can be represented in a principal component analysis by eigenvectors linking Fe II, $[\text{O III}]$, $\text{H}\beta$, and He II emission line properties and continuum properties, such as radio loudness, and the relative strength of X-ray emission, as characterized by α_{ox} (defined below). A recent, and possibly related result is that Seyfert 1 galaxies with broad $\text{H}\beta$ emission lines tend to have hard (flat) X-ray spectral slopes (see, e.g., Brandt, Mathur, & Elvis 1997). In a hard X-ray selected sample of (mostly Seyfert) AGNe, narrow $[\text{O III}]$ flux correlates well with X-ray flux, while broad Balmer lines do not (Grossan 1992). The physical origin of these diverse and interrelated correlations has yet to be determined.

We are launching a large-scale effort to probe these effects in large samples, using both data and analysis as homogeneous as possible. Many physically informative trends intrinsic to QSOs may be masked by dispersion in the data caused by either low signal-to-noise ratios or variability. An important tool for studying global properties of QSOs is the coaddition of data for samples of QSOs. In this

paper, we concentrate on an analysis of composite optical/UV spectra of subsamples of QSOs grouped by the relative strength of their soft X-ray emission.

2. ANALYSIS

2.1. Constructing Comparison Samples

Although the signal-to-noise ratio (S/N) for the individual spectra in both samples we study here tends to be about 10 or less per resolution element, the coaddition (averaging) of spectra with similar continuum properties allow us to increase the S/N and constrain the properties of the average QSO. Through averaging, a greater number of emission lines, with a wider range of ionization energies, and finer details in emission line profiles become measurable. This technique has been applied in several recent studies (see, e.g., Cristiani & Vio 1990; Francis et al. 1991; Osmer, Porter, & Green 1994; Zheng et al. 1996). What is lost is a reliable measure of the intrinsic dispersion in the observed correlations. However, it is important to first discover the correlations intrinsic to the average QSO. The sources of dispersion in the relationship can later be studied if data of adequate S/N are available for a large enough sample.

Table 1 summarizes mean continuum properties for the X-ray bright and X-ray faint subsamples we culled from the Large Bright Quasar Survey and *IUE* QSO samples described below. Optical and X-ray luminosities are taken from Green et al. (1995) and Green (1996) and assume $H_0 = 50 \text{ km s}^{-1} \text{ Mpc}^{-1}$ and $q_0 = 0.5$. The slope of a hypothetical power law connecting 2500 Å and 2 keV is defined as $\alpha_{\text{ox}} = 0.384 \log(l_{\text{opt}}/l_{\text{x}})$, so that α_{ox} is larger for objects with stronger optical relative to X-ray emission.

2.1.1. LBQS Sample

The Large Bright Quasar Survey (LBQS; Hewett, Foltz, & Chaffee 1995) is a sample of more than 1000 QSOs, uniformly selected over a wide range of redshifts. LBQS QSO candidates were selected using the Automatic Plate Mea-

suring Machine (Irwin & Trimble 1984) to scan UK Schmidt direct photographic and objective prism plates. A combination of quantifiable selection techniques were used, including color selection, selection of objects with strong emission lines, and selection of objects having redshifted absorption features or continuum breaks. The technique appears to be highly efficient at finding QSOs with $0.2 < z < 3.3$, a significantly broader range than in past work. Follow-up (6–10 Å resolution) optical spectra with $S/N \approx 10$ (in the continuum at ~ 4500 Å) were obtained at the Multiple Mirror Telescope (MMT) and the 2.5 m duPont telescope. The digital spectra used here were graciously provided to the author by Craig Foltz.

Soft X-ray data for LBQS QSOs was selected from the *ROSAT* All-Sky Survey (RASS) as detailed in Green et al. (1995). Of the 908 QSOs in the LBQS/RASS sample, 92 are detected in X-rays. For the nondetections, we assign an upper limit of 4σ to the raw counts.

Before generating composite spectra, we remove QSOs with known broad absorption lines (BAL QSOs) from the LBQS/RASS sample. Above $z = 1$, an insufficient fraction of QSOs are detected to construct X-ray bright and faint subsamples of comparable size. We therefore exclude QSOs with redshifts > 1 , for which the RASS data are insufficiently sensitive to be of use. To create composite spectra of similar S/N, we choose a dividing point of α_{ox} that results in similarly sized subsamples. We construct the X-ray bright sample (XB; 60 QSOs) of only detected objects, with $\alpha_{\text{ox}} < 1.475$. The X-ray faint sample (XF; 54 QSOs) includes both detections and lower limits with $\alpha_{\text{ox}} \geq 1.475$. QSOs with lower limits below that value could rightly belong either to the XB or XF sample and so are excluded from consideration. Note also that the value of 1.475 does not imply that α_{ox} is measured to such accuracy. Rather, it provides a convenient dividing line near the median of the small range of α_{ox} values (~ 1.2 – 1.6) typically measured in QSOs.

Continuum properties of the final XF and XB (α_{ox} -selected) samples are listed in Table 1. In survival analysis, if the

TABLE 1
CONTINUUM PARAMETERS FOR QSO SUBSAMPLES

PARAMETER	SUBSAMPLE	SAMPLE SIZE		MEDIAN	MEAN	RMS	TRUNCATED ^b	PROBABILITY ^c (%)
		N_{total}	$N_{\text{limits}}^{\text{a}}$					
Redshift	LBQS/XF	54	0	0.46	0.49	0.03	No	43
	LBQS/XB	60	0	0.45	0.51	0.03	No	
	<i>IUE</i> /XF	23	0	0.35	0.57	0.09	No	2.5
	<i>IUE</i> /XB	25	0	0.21	0.34	0.03	No	
$\log l_{\text{opt}}$	LBQS/XF	54	0	30.41	30.44	0.06	No	17
	LBQS/XB	60	0	30.30	30.30	0.06	No	
	<i>IUE</i> /XF	23	0	31.03	31.05	0.15	No	25
	<i>IUE</i> /XB	25	0	30.50	30.57	0.08	No	
α_{ox}	LBQS/XF	54	42	1.61	1.61	0.01	1.67	$< 10^{-4}$
	LBQS/XB	60	0	1.34	1.35	0.01	No	
	<i>IUE</i> /XF	23	4	1.57	1.60	0.03	No	$< 10^{-4}$
	<i>IUE</i> /XB	25	0	1.31	1.28	0.02	No	
$\log l_{\text{x}}$	LBQS/XF	54	42	22.55	25.96	0.08	25.64	$< 10^{-4}$
	LBQS/XB	60	0	26.78	26.78	0.06	No	
	<i>IUE</i> /XF	23	0	26.91	26.78	0.20	No	1
	<i>IUE</i> /XB	25	0	27.17	27.25	0.09	No	

NOTE.—For LBQS/XF, $z < 1$ and $\alpha_{\text{ox}} \geq 1.475$; for LBQS/XB, $z < 1$ and $\alpha_{\text{ox}} < 1.475$, detections only; for *IUE*/XF, $\alpha_{\text{ox}} \geq 1.4$; and for *IUE*/XB, $\alpha_{\text{ox}} < 1.4$, detections only.

^a All limits are upper limits except for α_{ox} .

^b This column lists the value of an outlying nondetection, if it was necessarily redefined, truncating the distribution to allow normalization. The resulting mean value is biased.

^c Probability that the two subsample distributions for this parameter are randomly drawn from the same parent distribution, from ASURV logrank test.

TABLE 2
COMPOSITE NORMALIZATION DEFINITIONS

Wavelength Region	λ_n	Continuum Band	Continuum Band	Line Name
LBQS Spectra				
4150–5100	4863	4710–4780	5040–5090	H β
3800–4800	4102	4020–4050	4150–4270	H δ
3200–4000	3426	3360–3400	3450–3500	[Ne v]
2000–3000	2798	2645–2700	3020–3100	Mg II
IUE Spectra				
1000–2000	1549	1450–1480	1680–1700	C IV

NOTE.—Each individual rest-frame QSO spectrum is divided by the flux of the fit line at the normalization wavelength λ_n before addition to a composite spectrum. The continuum level at λ_n is found by fitting a linear continuum between two points, the mean flux values in the two continuum bands shown, at their central wavelength points.

lowest (highest) point in the data set is an upper (lower) limit, the mean is not well defined since the distribution is not normalizable, and so the outlying censored point is redefined as a detection. For the XF sample, we list here the value of that redefined limit at which the distribution is truncated. The resulting mean value is biased, so that the true mean values of α_{ox} and $\log l_x$ for the LBQS XF sample are probably even more X-ray faint than those listed.

We find no significant differences in the distributions of redshift, $N_{\text{H}}^{\text{Gal}}$, or l_{opt} between our XB and XF subsamples of the LBQS. In any case, the emission line properties of the LBQS as a whole show no strong dependence on either luminosity or redshift (Francis, Hooper, & Impey 1993).

2.1.2. IUE Sample

To explore changes in QSO UV spectra as a function of α_{ox} , we include a previously compiled sample of QSOs

observed by both the *International Ultraviolet Explorer* (IUE) and *Einstein*. This sample was selected as described in Green (1996), by requiring that the QSOs in the IUE sample have *Einstein* soft X-ray data available. In Wilkes et al. (1994), we define the IUE/*Einstein* sample of 49 objects.

Again, we remove all known BAL QSOs from the IUE sample. With this sample, because of selection effects, it is not possible to achieve similar-sized subsamples with similar redshift distributions by selecting an appropriate α_{ox} value at which to divide the sample. Similar redshift distributions are obtained for $\alpha_{\text{ox}} = 1.3$, but then the XB subsample contains only about a dozen QSOs, compared to 37 in the XF subsample. Similar subsample sizes are obtained for $\alpha_{\text{ox}} = 1.4$, for which, however, the requirement of a detection in the XB sample results in a lower mean redshift, due mostly to extra QSOs between $0.1 < z < 0.2$. Since QSO spectral evolution between their mean redshifts (0.34 and 0.57, respectively) is negligible, we emphasize the subsample's split at $\alpha_{\text{ox}} = 1.4$, which is in any case closer to the dividing value for the LBQS subsamples. However, we also check the subsample's split at $\alpha_{\text{ox}} = 1.3$ to ensure that evolu-

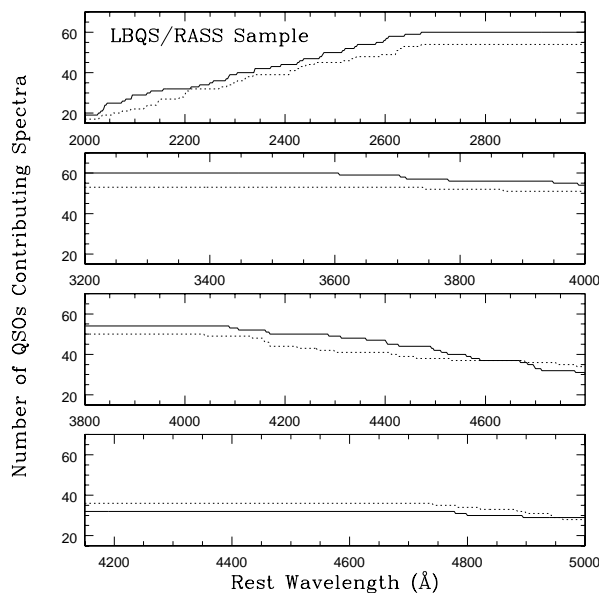


FIG. 1.—Histograms of the number of QSOs whose spectra contribute to each of eight LBQS composite spectra. Four separate continuum points were used to generate LBQS composite spectra for XB and XF subsamples in four separate wavelength regions (see Table 2). Composites normalized at the four different continuum points have different histograms, since they require the rest frame continuum bands to be present in all contributing observed frame spectra. Different selection criteria for the XB (solid lines) and the XF subsamples (dotted lines) also yield slightly different histograms.

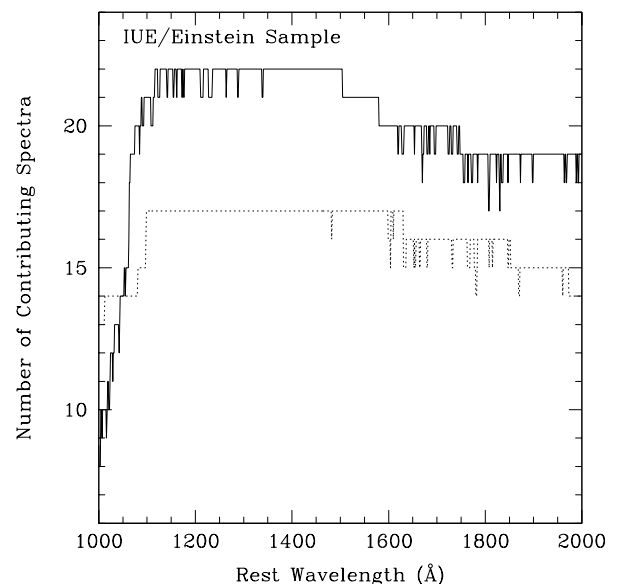


FIG. 2.—Histograms of the number of QSOs whose spectra contribute to the IUE composite spectra for the XB subsample (solid line) and the XF subsample (dotted line). The IUE composites were all normalized at the rest wavelength of C IV.

tion or luminosity effects do not significantly bias our results.

2.2. Constructing Composite Spectra

We first deredshift each individual spectrum by dividing the linear dispersion coefficients (initial wavelength and wavelength per pixel) by $(1+z)$. An estimate of the rest frame continuum flux $f_{c,l}$ at a chosen normalization point is then derived by fitting a linear continuum between two continuum bands. The widths and centers of these bands, typically chosen to straddle an important emission line, are listed for each wavelength region in Table 2. We then normalize the entire spectrum via division by $f_{c,l}$.

Each normalized spectrum is first rebinned to the dispersion of the composite spectrum, conserving flux via interpolation. We choose 2.5 \AA bins, similar to the majority of the individual LBQS spectra. The *IUE* spectra are binned to 1.18 \AA , as in the original short-wavelength prime (SWP) camera spectra. Each normalized, rebinned spectrum is then stored as a vector in a two-dimensional array. Finally, for each pixel in the completed array, the number of spectra N with fluxes in that rest frame wavelength bin is tallied. If $N \geq 3$, the median and the mean of all the flux values in the bin are computed and stored in the final one-dimensional composite spectra, as is N in the final histogram array. A similar procedure is performed for each bin, until the spectra are completed. The strong sky line at $\lambda 5577$, sometimes poorly subtracted, was omitted from the LBQS composite. Geocoronal Ly α lines were similarly excluded when building the *IUE* composites.

We chose four separate continuum points to generate LBQS composite spectra in four wavelength regions (Table 2). Composites normalized at different continuum points may have different histograms, since they require the rest frame continuum bands to be present in all contributing observed frame spectra. Histograms of the number of QSOs contributing to each LBQS composite are shown in Figure 1. The *IUE* composites were all normalized at the wavelength of C IV, and the histograms for those spectra are shown in Figure 2.

The median composites appear to be smoother than the means, since they are less affected by spikes and low S/N features in the individual spectra. As a result, the χ^2 values of model fits are also lower for median composites. However, since the median omits QSOs with more extreme spectral properties, we prefer to analyze the average composites. We check the significance of every strong difference between XB and XF average composites by measurement of the median composites to determine whether outliers dominate the feature in question.

3. EMISSION LINE MEASUREMENTS: LBQS

No analysis of continuum slope is presented for the LBQS spectra, since these observations are not fully spectrophotometric. Using the IRAF task SPECFIT (Kriss 1994), we fit simple empirical models to the LBQS composite spectra in four wavelength regions, defined in Table 2. In each region, we begin by fitting a power-law (PL) continuum using only comparatively line-free regions (listed for each region below). The resulting continuum fit parameters are slope α and intercept f_{1000} , such that flux $f_\lambda = f_{1000}(\lambda/1000)^\alpha$. Since the LBQS spectra are not spectrophotometric, the continuum fit results should be used only to derive exact composite equivalent widths from

(normalized) line fluxes if desired. The intercept value reflects the arbitrary normalization of individual spectra to unity at the chosen wavelength λ_n shown in Table 2.

The emission line components are assumed to be Gaussian and symmetric (skew fixed at unity), so output from the fits includes flux, centroid, and FWHM for each line. Results from these fits are shown in Table 3 and Figure 3. The errors listed in both Tables 3 and 4 are directly from the SPECFIT task, which assumes that the errors on the input spectrum follow a Gaussian distribution. The tabulated errors represent 1σ for a single interesting parameter.

3.1. The H β and [O III] Region

We fit a PL continuum using these relatively line-free regions: $\lambda\lambda 4020\text{--}4050$, $4150\text{--}4270$, $4420\text{--}4450$, $4710\text{--}4780$, and $5070\text{--}5130$. The resulting fit parameters are fixed, while the following single Gaussian components are fit to the strong emission lines between 4150 to 5100 \AA : (1) broad H β ; (2) narrow H β , with FWHM fixed to that of [O III] $\lambda 5007$; (3) [O III] $\lambda 5007$; and (4) [O III] $\lambda 4959$, fixed relative to the central wavelength and $(1/3)$ flux of component (3). Finally, the blended iron emission above the PL continuum is summed over the wavelength range $\lambda\lambda 4434\text{--}4684$.

As can be seen from Figure 3 and Table 3, by far the strongest effect is the great relative strength of [O III] emission in the XB composite; [O III] emission is ~ 2.5 times stronger in X-ray bright sample. Broad H β emission is about 40% stronger in the XB composite, although the FWHM are similar at $\sim 5700 \text{ km s}^{-1}$. The strengths of the narrow components of H β are comparable. In both XB and XF composites, broad H β is redshifted relative to rest (i.e., relative to [O III] $\lambda 5007$ or narrow H β) by about 300 km s^{-1} .

Boroson & Green (1992; hereafter BG92), in a principal component analysis of low-redshift QSO spectra, found that the principal eigenvector of their sample (the linear combination of parameters that represents the largest variance in the sample) is primarily an anticorrelation between the strength of [O III] emission and optical Fe II strength. This trend is in the same direction as we find here, with the large W_λ ([O III]) XB sample having the lower Fe II equivalent width, as judged by the iron emission near $\lambda 4600$ (Table 3).

We can make more precise measurements in this region if we subtract Fe II emission. Marianne Vestergaard has accomplished this task, using a technique similar to that of BG92. A narrow optical Fe II template spectrum (of IZw1; BG92) is convolved with a Gaussian function and subtracted from the LBQS composites, fitting iteratively by eye. The flux in the iron template between $\lambda 4434$ and $\lambda 4684$ is within $\sim 10\%$ of that found via our simple summation technique. Because of a strong iron multiplet with lines at $\lambda\lambda 4924$, 5015 , and 5169 , however, subtraction of Fe II decreases the apparent W_λ ([O III]) in both the XF and XB composites. In the XF composite, where iron emission is strong, the measured W_λ ([O III]) at $\lambda 5007$ decreases from 13.5 to 7.5 , and its measured FWHM decreases from 1330 to 650 km s^{-1} . The XF H β line changes by comparison only slightly after iron subtraction (from a total equivalent width of 53 to 47). In the XB composite, where iron emission is weak, the measured change in equivalent width of both [O III] and H β after Fe II subtraction are within the errors ($\Delta W_\lambda < 3 \text{ \AA}$), as are the changes in FWHM. Since the strength of [O III] in the XF composite is initially low, the

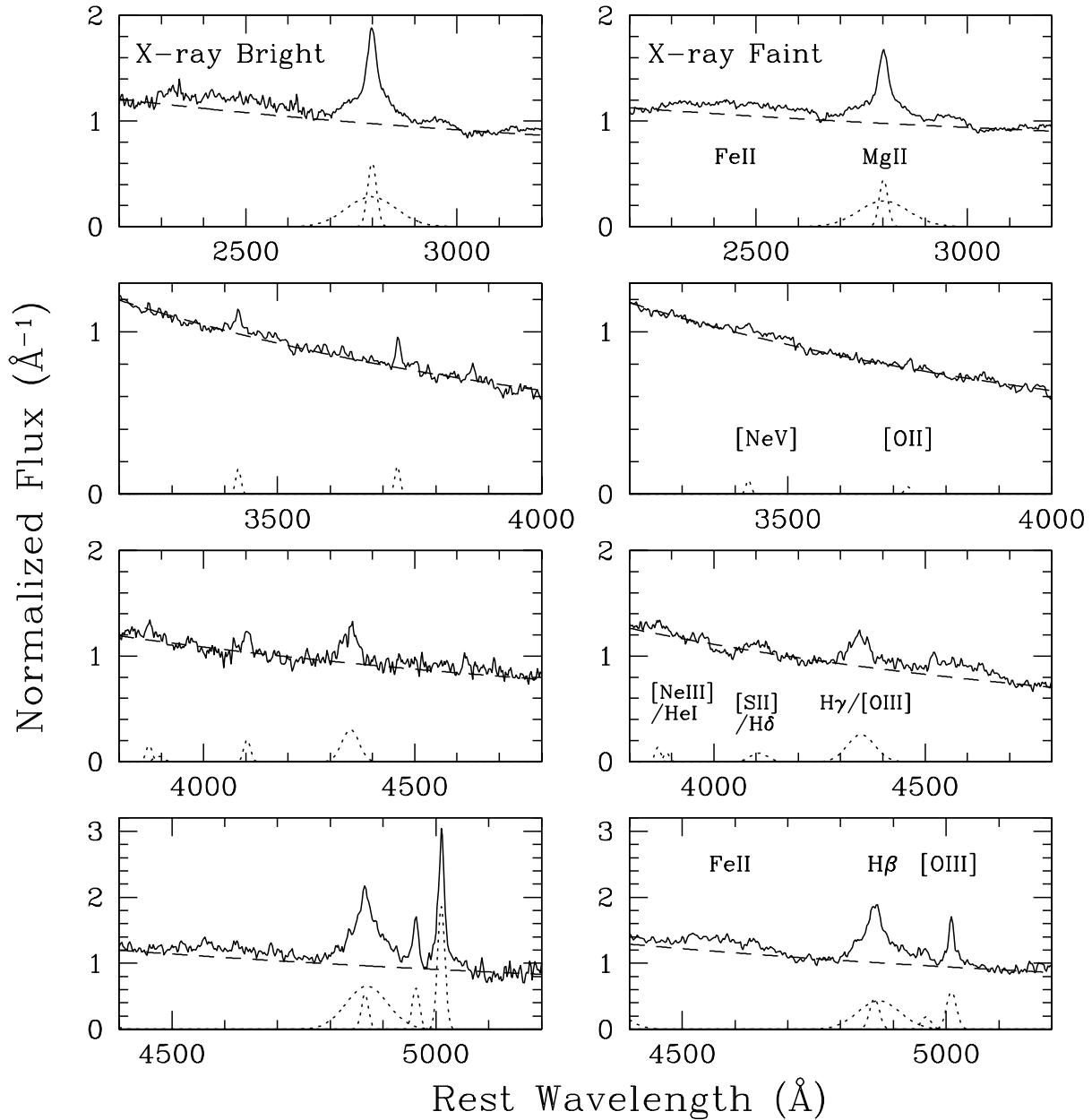


FIG. 3.—Final normalized composite spectra of the LBQS sample. The left-hand column contains plots of the XB composites, while the right-hand column shows XF composites. Each row shows a portion of a composite constructed from spectra normalized at a different rest wavelength continuum point (see Table 2): $\lambda 2798$ (top row), $\lambda 3426$ (second row), $\lambda 4102$ (third row), and $\lambda 4863$ (bottom row). Individual lines and their parameters measured using SPECFIT (Kriss 1994) are listed in Table 3. Fitted components are shown in each plot. These include the best power-law continuum fit to relatively line-free continuum regions (dashed lines) and Gaussian emission lines (dotted lines). Lines are identified by name in the X-ray faint plots.

difference in the measured $[\text{O III}]/\text{H}\beta$ ratio between XF and XB composites is substantially increased by Fe II subtraction. Much smaller effects are expected on other emission lines treated here. An important extension of this technique to the UV will be described in an upcoming paper (Vestergaard & Green 1998).

3.2. The $\text{H}\delta$ Region

First, we fit a PL continuum through the windows: $\lambda\lambda 3790\text{--}3845$, $4020\text{--}4050$, $4150\text{--}4270$, $4420\text{--}4450$, and $4710\text{--}4780$. Gaussian components are fit between 3800 and 4800 Å to the following lines: $[\text{Ne III}]\ \lambda 3869$, $\text{He I}\ \lambda 3889$, $[\text{S II}]/\text{H}\delta\ \lambda\lambda 4068/\lambda\lambda(4076 + 4102)$, and $\text{H}\gamma/[\text{O III}]\ \lambda\lambda(4340 + 4363)$. The only significant difference seen

between emission lines in this region is that the $\text{H}\gamma/[\text{O III}]$ blend is *stronger* (at the $2.7\ \sigma$ level) in the XF composite.

3.3. The $[\text{Ne v}]$ and $[\text{O II}]$ Region

Line-free regions at $\lambda\lambda 3200\text{--}3400$, $3500\text{--}3700$, and $3800\text{--}4000$ are used for the PL fit. Then single Gaussian components are fit for $[\text{Ne v}]\ \lambda 3426$ and $[\text{O II}]\ \lambda 3727$. As can be seen from Figure 3 and Table 3, both the $[\text{Ne v}]$ and $[\text{O II}]$ line fluxes are much stronger in the XB composite, consistent with the relative strengths of other unblended narrow lines measured. For the XF sample, the very weak $[\text{O II}]$ line could not be successfully fit when leaving both λ_c and FWHM free to vary, so we fixed the central wavelength at 3727 Å. Similarly, the weakness of $[\text{Ne v}]$ demanded that its

TABLE 3
SPECFIT RESULTS FOR LBQS COMPOSITES

Component	Parameter	XB Composite	XF Composite
2000–3000 Å continuum	f_{1000}	2.44 ± 0.07	1.79 ± 0.04
	α	0.89 ± 0.03	0.59 ± 0.02
	f^a	41.1 ± 0.2	36.8 ± 0.1
Fe II	f	42.0 ± 2.5	36.4 ± 2.1
Mg II broad ^b	λ_c	2796.9 ± 3.5	2801.6^c
Mg II narrow	f	15.94 ± 1.38	11.26 ± 1.11
	λ_c	2798.8 ± 0.8	2801.6 ± 0.8
	FWHM	2650 ± 230	2530 ± 240
3200–4000 Å continuum	f_{1000}	31.3 ± 1.2	29.2 ± 0.8
	α	2.81 ± 0.03	2.76 ± 0.02
	f	1.89 ± 0.22	1.06 ± 0.15
Ne V ^d	λ_c	3425.6 ± 1.2	3425.5 ± 1.8
[O II] ^e	f	2.10 ± 0.24	0.65 ± 0.17
	FWHM	900 ± 120	1090 ± 290
3800–4800 Å continuum	f_{1000}	13.5 ± 1.3	35.6 ± 3.1
	α	1.82 ± 0.07	2.50 ± 0.06
	f	2.9 ± 1.2	2.3 ± 0.6
[Ne III]	λ_c	3870.8 ± 3.6	3867.3 ± 4.1
	FWHM	1330 ± 240	1200^f
	f	1.45 ± 1.3	1.43 ± 0.6
He I	λ_c	3894 ± 15	3887 ± 6
	FWHM	2100 ± 1500	1200^f
	f	4.06 ± 0.6	4.10 ± 1.0
[S II] + H δ	λ_c	4103.0 ± 1.5	4106.7 ± 6.1
	FWHM	1330 ± 240	3440 ± 780
	f	15.3 ± 1.0	20.7 ± 1.7
H γ + [O III]	λ_c	4347.5 ± 1.5	4348.4 ± 2.8
	FWHM	3240 ± 250	5200 ± 620
	f_{1000}	30.0 ± 3.3	47.0 ± 3.4
4150–5100 Å continuum	α	2.17 ± 0.07	2.43 ± 0.05
	f^g	26.5 ± 0.2	31.1 ± 0.1
	f	64.0 ± 2.6	42.8 ± 2.5
Fe II	λ_c	4869.3 ± 1.7	4872.5 ± 2.5
	FWHM	5660 ± 290	5730 ± 360
	f	9.1 ± 1.4	10.7 ± 1.7
H β broad	λ_c	4865.6 ± 1.1	4864.2 ± 1.3
	FWHM ^h	976	1330
	f	32.32 ± 1.11	13.46 ± 0.95^i
H β narrow	λ_c	5010.2 ± 0.3	5009.9 ± 0.8
	FWHM	976 ± 43	1330 ± 108
	[O III] $\lambda 5007$		

NOTE.—All fluxes are summed over a locally normalized continuum (see text) and so are approximately equivalent widths. The value of the (normalized) continuum flux at any wavelength λ can be obtained via $f_c = f_{1000} (\lambda/1000)^{-\alpha}$. Emission line centroids λ_c are in Å, while FWHM are shown in km s⁻¹.

^a Fe II summed over PL fit from $\lambda\lambda 2210$ – 2730 .

^b FWHM fixed at $15,000$ km s⁻¹.

^c λ_c fixed at narrow Mg II values.

^d FWHM fixed at 1000 km s⁻¹.

^e λ_c fixed at 3727 Å.

^f FWHM fixed at 1200 km s⁻¹.

^g Fe II summed over PL fit from $\lambda\lambda 4434$ – 4684 .

^h FWHM fixed at [O III] $\lambda 5007$ FWHM.

ⁱ W_λ ([O III]) of XF composite decreases to 7.5 ± 1 after Fe II subtraction.

FWHM be fixed because otherwise SPECFIT seeks to fit neighboring features with an unrealistically broad line. The use of composite spectra enables us here for the first time to show that these narrow lines are about 3 times as strong in the X-ray bright QSOs as in their X-ray faint analogs.

3.4. The Mg II Region

Here a PL continuum is fit to $\lambda\lambda 2195$ – 2275 , 2645 – 2700 , and 3020 – 3100 windows. The spectrum from 2000 to 3200 Å is then fit with the fixed PL plus these Gaussian components: narrow Mg II and broad Mg II, fixed in wavelength to the narrow component. Without fixing the broad line width, the fit would wander off trying to include nearby blended iron lines. Finally, the blended iron emission above

the PL continuum is summed over the wavelength range 2210 – 2730 Å.

We find here that the XB sample has stronger UV Fe II emission (Table 4), opposite to the trend for optical Fe II. Green et al. (1995) also found that QSOs in the LBQS with strong UV Fe II emission are particularly bright in the soft X-ray bandpass. UV Fe II lines have their principal ionizing and heating continuum above 500 eV; Fe II lines in the optical are principally caused by continuum above 800 eV.

4. EMISSION LINE MEASUREMENTS: IUE

For the IUE spectra, convincing model fits to the composite spectra could be obtained when fitting a simple PL continuum simultaneously with lines. The following single

TABLE 4
SPECFIT RESULTS FOR *IUE* COMPOSITES

Component	Parameter	XB Composite	XF Composite
1000–2000 Å continuum.....	α	1.51 ± 0.02	1.57 ± 0.02
Ly β /O VI	f_{1000}	0.75 ± 0.02	0.75 ± 0.03
	f	19.6 ± 1.1	10.1 ± 1.0
	λ_c	1033.5 ± 0.4	1032.5 ± 0.6
Ly α broad	FWHM	5230 ± 400	4560 ± 450
	f	87.3 ± 3.9	78.7 ± 2.9
	λ_c	1218.8 ± 0.8	1218.7 ± 0.5
Ly α narrow	FWHM	12840 ± 410	12700 ± 400
	f	47.3 ± 1.7	36.8 ± 2.2
	λ_c	1214.6 ± 0.1	1214.9 ± 0.2
N V	FWHM	3030 ± 80	3470 ± 130
	f	3.9 ± 2.5	1.2 ± 0.3
	λ_c	1240 ± 3	1244 ± 1
O I	FWHM	6000 ± 1200	6700 ± 3200
	f	2.6 ± 0.9	6.8 ± 1.9
	λ_c	1310 ± 4	1312 ± 4
S IV	FWHM	6700 ± 3400	6400 ± 2100
	f	8.4 ± 1.0	11.2 ± 1.6
	λ_c	1398 ± 1.7	1395 ± 2.3
C IV broad	FWHM	6250 ± 870	6270 ± 950
	f	52.9 ± 1.3	39.2 ± 9.0
	λ_c	1546.2 ± 1.6	1548.3 ± 1.6
C IV narrow	FWHM	12500 ± 2800	12000 ± 2500
	f	30.6 ± 6.6	14.8 ± 7.9
	λ_c	1549.09 ± 0.2	1548.34 ± 0.6
Absorption	FWHM	3200 ± 350	3400 ± 940
	f	5.8 ± 3.9	8.8 ± 1.4
	λ_c	1487 ± 19	1480 ± 12
	FWHM	12900 ± 1800	12500 ± 2800

NOTE.—Parameters have the same meaning as in Table 3.

Gaussian components are fit to the spectrum between 1000 and 2000 Å: (1) Ly β /O VI, (2) broad Ly α , (3) narrow Ly α , (4) N V, (5) O I, (6) S IV, (7) broad C IV, (8) narrow C IV, and (9) C IV absorption. Again, Gaussian components are assumed to be symmetric. The data do not warrant multiple Gaussian fits to lines as weak or weaker than N V. However, some such lines are included in the fit partly to insure that a reasonable continuum estimate is derived.

Results from these fits, shown in Table 4 and Figure 4, are described below.

1. The PL continuum fits are similar in slope. At the 2σ level, the XF sample may be marginally steeper. If verified in other samples, this could be caused by reddening or absorption by dust. However, the similarity of the slopes suggests that the relative attenuation between the XB and XF spectra is gray.

2. Just as for the LBQS composites, we find for the *IUE* sample that line emission is significantly stronger in the XB composite. Ly β /O VI, Ly α , and C IV, when fit with a single Gaussian component, are each significantly ($> 3\sigma$) stronger in the XB composite. For Ly α , the narrow/broad line flux ratios are higher in the XB composite as well. Some marginal evidence ($\sim 1.5\sigma$) for the same effect is seen for C IV.

From Table 4, it is clear that the Ly β /O VI emission line shows a large contrast. The inverse correlation between Ly β /O VI and α_{ox} was also remarked recently in a sample of individual *Hubble Space Telescope* (*HST*) Faint Object Spectrograph (FOS) spectra (Zheng, Kriss, & Davidsen 1995). Among weaker emission lines, O I λ 1302 and Si IV/O IV] show a marginal ($< 2\sigma$) trend in the opposite direction, with smaller W_λ in the XB composite. There is also a

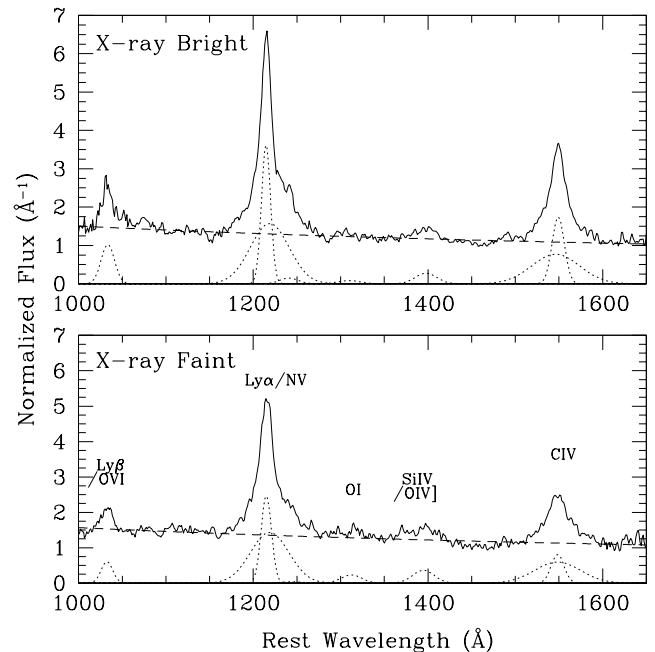


FIG. 4.—Final normalized composite spectra of the *IUE*/*Einstein* sample. The top plot is the XB composite, and the bottom shows the XF composite. Both these *IUE* composites were constructed from spectra normalized at $\lambda 1549$, the rest wavelength of C IV. Individual lines and their measured parameters using SPECFIT (Kriss 1994) are listed in Table 4. The best-fit components are shown in each plot. These include a power-law continuum (dashed lines) fit simultaneously with Gaussian emission lines (dotted lines). Lines are identified by name in the X-ray faint plot. Note the apparent continuum deficit centered near $\lambda 1480$ in the XF composite.

suggestion that in the XF composite, N v is weak or non-existent. These should be investigated at higher S/N.

3. There is marginal evidence for a continuum flux deficit blueward of C iv of the XF continuum.

4.1. Evidence for Absorption

It proved difficult to fit the *IUE* XF spectrum with a convincing PL continuum because of a dip blueward of the C iv emission line, which we tentatively interpret as absorption. We fit a simple Gaussian component to the absorption, which is sufficient to characterize the absorbed flux and velocity width. The result is that the C iv emission line fits remain unchanged while the overall fit improves, but only for the XF spectrum. (The formal improvement in χ^2 would appear marginal because the absorbed region covers only a few percent of the spectrum.) The equivalent width (W_λ) of the absorption is $8.8 \pm 1.4 \text{ \AA}$, centered at $1480 \pm 10 \text{ \AA}$, with an FWHM of $12,500 \pm 2800 \text{ km}^{-1}$ (see Table 4). Some evidence for a similar dip can be seen even in the XB spectrum, but it is smaller, and its W_λ is not significant in the fit in comparison to the formal errors ($< 1.5 \sigma$).

If individual absorbers contribute to the dip in the *IUE* XF composite, they are likely to be narrow, weak, and undetected in the noise of the individual spectra. When the spectra of XF QSOs are combined, however, the enlarged width and higher S/N of the composite absorber could enable detection of a broad feature. High-velocity intrinsic narrow-line absorption in QSOs is just now being recognized in individual QSOs (Hamann et al. 1997); the challenge is to properly distinguish it from intervening absorption.

In summary, there is evidence for a dip blueward of the C iv emission line in the XF composite, independent of any reasonable continuum choice. If the dip in the XF composite is caused by C iv absorption, the absorber is highly ionized and is probably situated near the ionizing source. The large velocity width also suggests proximity to the broad-line region (BLR). The weak X-ray emission combined with evidence for high-velocity ionized absorbers is reminiscent of recent results associating soft X-ray and UV absorption (Mathur 1994; Mathur, Elvis, & Wilkes 1995; Green & Mathur 1996; Green et al. 1997).

5. DISCUSSION

We now consider a variety of possibilities to account for the optical and UV spectral difference between X-ray bright and X-ray faint QSOs: (1) luminosity effects, (2) radio loudness, (3) absorption, and (4) changes in the *intrinsic* spectral energy distribution (SED). The strength of some of these effects is directly testable using the samples at hand.

5.1. Luminosity Subsamples

Both selection effects and secondary correlations must be considered when evaluating the significance of observed correlations such as these. Two well-known effects could conspire to produce an overall weakening of emission lines with increasing α_{ox} . First, α_{ox} is known to increase with optical luminosity (Wilkes et al. 1994; Green et al. 1995), at least for optically selected samples (LaFranca et al. 1995). Secondly, as luminosity increases, line equivalent width decreases (i.e., the Baldwin effect; Baldwin 1977). Could these effects combine to produce the anticorrelation of α_{ox} and line strength observed here?

As can be seen from Table 1, the LBQS subsamples are well matched in optical luminosity, so that no Baldwin effect is expected. Furthermore, the strength of the Baldwin effect in the optical is known to be weak.

Our results from the *IUE* subsamples are less immune to a Baldwin effect/SED conspiracy because our *IUE* subsamples are not as well matched in luminosity and because the Baldwin effect is much stronger in the UV. We therefore perform a stringent check, applying the same spectral averaging techniques now to new subsamples defined by UV luminosity.

We divided the *IUE* sample at the mean UV luminosity¹ value of 30.6. The resulting low UV luminosity (UVLO; 27 QSOs) and high UV luminosity (UVHI; 22 QSOs) subsamples both had mean $\alpha_{\text{ox}} = 1.4 \pm 0.04$. SPECFIT procedures identical to those of the XB and XF samples were applied. Virtually all spectral differences were *less* significant in the UV luminosity subsamples than in the α_{ox} subsamples. Only narrow Ly α emission changes more strongly between UV subsamples than between the α_{ox} subsamples. Indeed, the Baldwin effect appears to be strongest in the narrow-line components of both Ly α and C iv. The bulk of the effect could be caused by differences in narrow-line region (NLR) emission, as was also suggested by Osmer et al. (1994).

Since emission line correlations are stronger with α_{ox} than with luminosity, we conclude that either (1) W_λ depends primarily on the *shape* of the ionizing continuum, crudely characterized here by α_{ox} , or (2) both W_λ and α_{ox} are related to some third parameter characterizing the QSO physics. One such possibility is absorption.

Could the correlation of α_{ox} to luminosity *cause* the Baldwin effect? Although by design we have selected subsamples of similar luminosity for our XF and XB composites, we may suppose that the primary relationship between W_λ and α_{ox} is propagated into the relationship between α_{ox} and luminosity, and we test the strength of the predicted secondary relationship between W_λ and luminosity that results, i.e., the Baldwin effect.

We begin by simply contrasting the observed response here of W_λ (C iv) and W_λ (Mg II) to α_{ox} with that predicted in the most recent comprehensive study of the Baldwin effect in optically selected QSOs (Zamorani et al. 1992). The change $\Delta \overline{\alpha_{\text{ox}}} \sim 0.3$ between XF and XB subsamples is similar in our *IUE* and LBQS samples. The change in $\log W_\lambda$ (Mg II) predicted by the BEff in this line is $\Delta \log W_\lambda$ (Mg II) $\sim -0.68 \alpha_{\text{ox}} = 0.18$. The change we actually measure between XB and XF composites is (from the values in Table 3) $\Delta \log W_\lambda$ (Mg II) = 1.0. Similarly, the change predicted by the BEff in $\log W_\lambda$ (C iv) seen by Zamorani et al. is $\Delta \log W_\lambda$ (C iv) $\sim -1.16 \alpha_{\text{ox}} = 0.30$, while we actually measure $\Delta \log W_\lambda$ (C iv) = 1.57. Thus, the effect of α_{ox} on emission line strengths is some 5–6 times larger than that expected if it were secondary to a luminosity effect. Indeed, *it seems likely that the BEff is secondary to the relationship between α_{ox} and line equivalent width.*

If the BEff is caused by a change in α_{ox} concomitant with luminosity, then the strongest W_λ (α_{ox}) relationship we see, that of W_λ ([O III]), predicts a BEff in [O III]. This is indeed seen in the BG92 data, where the probability of no correlation (the null hypothesis) between M_V and W_λ ([O III]) $\lambda 5007$ is $< 1\%$.

¹ The log rest frame luminosity, $\log l_{\text{UV}}$, in $\text{ergs cm}^{-2} \text{ s}^{-1} \text{ Hz}^{-1}$ at 1450 \AA , is defined in Green (1996).

5.2. Radio Properties

Radio and X-ray loudness are correlated; Green et al. (1995) confirmed that radio loud QSOs (RLQs) are more soft X-ray luminous than radio quiet QSOs (RQQs) in the LBQS. Unfortunately, the difference in radio loudness between the LBQS XF and XB subsamples cannot be well characterized: although 4 (of 17 with radio data) are radio detected in the LBQS XB subsample, only one QSO (of 38) in the XF subsample is a radio detection.

However, OUV spectral differences as a function of radio loudness have been extensively studied. Differences between emission lines in RLQ and RQQ spectra longward of 1600 Å are quite subtle, and there is a remarkable similarity in Mg II and C III] emission lines between RLQs and RQQs (Francis et al. 1993). Distinctions found by BG92 include a redward asymmetry of H β in RLQs, whereas RQQs show about equal numbers of red and blue asymmetries (BG92). Radio loud QSOs tend to have strong [O III] and weak optical Fe II. In Wang, Brinkmann, & Bergeron (1996), neither H β nor optical Fe II measurements correlate with radio loudness.

To check the effects of radio loudness on UV emission lines, we created radio loud (RL) and radio quiet (RQ) composite UV spectra from the *IUE/Einstein* sample. We determined radio loudness from Falcke, Sherwood, & Patnaik (1996) for all the UV-excess selected (PG) QSOs, and from Veron-Cetty & Veron (1993) or the NED database for others. Two QSOs are omitted because of intermediate radio loudness, and two more have no published radio data. Radio subsamples are identical in luminosity and well matched in redshift if we impose $z > 0.15$. This yields $N = 26$ and $\bar{z} = 0.48$ for the RL subsample, $N = 13$ and $\bar{z} = 0.52$ for RQ QSOs, and $\log l_{\text{opt}} = 30.9$ for both. There is some remaining difference between α_{ox} distributions for the *IUE/Einstein* radio subsamples, as expected, such that the RL sample is somewhat more X-ray bright ($\bar{\alpha}_{\text{ox}} = 1.36 \pm 0.04$) than the RQ sample ($\bar{\alpha}_{\text{ox}} = 1.47 \pm 0.05$).

We find Ly α emission to be somewhat stronger in the RQ composite. C IV emission is of similar strength and FWHM in both RQ and RL composites but is displaced slightly to the red in the RL composite. Similar results were found independently by Wills & Brotherton (1995). Thus, overall, the emission line trends due to radio loudness in our sample are weaker than, and tend to *diminish*, those seen in α_{ox} . The important result is that *spectral differences between composites binned by α_{ox} are significantly larger than between composites binned by radio loudness.*

5.3. Absorption and the $\alpha_{\text{ox}}(l_{\text{opt}})$ Relation

Absorption by ionized gas near the nucleus can extinguish soft X-ray emission without having significant effects on the observed optical emission. The BAL QSOs represent an extreme example, wherein observed soft X-ray fluxes are at least an order of magnitude below those of non-BAL QSOs of similar optical brightness (Green & Mathur 1996). Even AGNe with much less spectacular UV absorption (e.g., narrow absorption lines) show significant soft X-ray absorption (Mathur 1994; Mathur et al. 1995). Since most QSOs have either low S/N, low resolution, or no available UV spectra, many such absorbers await recognition in current QSO samples.

Is it possible that the $\alpha_{\text{ox}}(l_{\text{opt}})$ correlation is itself caused by absorption? The hypothesis might be tested if *all* types of absorbed QSOs were removed, including QSOs with

known narrow-line intrinsic, damped Ly α , and Ly α forest absorbers. A higher S/N sample that has been systematically searched for absorption in both UV and soft X-ray spectra is needed. We are building such a sample from the *HST* FOS and *ROSAT* public archives and will study these issues in an upcoming paper.

We note that, if at least some of the correlation is caused by increased warm absorption at higher luminosities, then the correlation would be expected to be further weakened in soft X-ray selected samples. More common absorption in the UV bandpass is suspected anecdotally at higher luminosities but remains to be demonstrated statistically. In the X-ray bandpass, the same can be said for the popular assumption that absorption is *less* common at high luminosity. This latter notion should be particularly suspect, since higher energy rest frame X-ray emission is observed in most high-luminosity objects and requires a higher intrinsic absorbing column for detection. Furthermore, the most luminous objects in samples to date have also been radio loud (Reynolds 1997).

Variability may play a significant role in the $\alpha_{\text{ox}}(l_{\text{opt}})$ correlation. Typically, an optically selected AGN is found near the survey flux limit and therefore preferentially in a bright phase and then is later followed up in an X-ray-pointed observation. Overall, more distant (and thus more luminous) optically selected QSOs would tend to have larger measured α_{ox} . Even if variability-related biases are not responsible for the observed $\alpha_{\text{ox}}(l_{\text{opt}})$ correlation, such variability may be expected to introduce scatter into the true relation. As such, α_{ix} (the power-law spectral index between 1 μm and 2 keV) might prove a more variability-resistant measure. Indeed, Lawrence et al. (1997) have found that some of the primary correlations discussed here become more significant when α_{ix} replaces α_{ox} . Not only variability but also absorption more strongly affects the optical than the infrared.

5.4. Intrinsic Spectral Energy Distributions

We have offered one interpretation of our measurements that assumes that the *intrinsic* broadband continuum emission from the QSO central engine is constant in shape, independent of luminosity, but that the spectral energy distribution (SED) seen by the NLR and/or by us may be strongly affected by intervening, possibly ionized absorbing clouds. However, the change in α_{ox} , and the accompanying changes in emission lines may at least in part be caused by changes in the intrinsic SED.

Many QSOs have soft ($\lesssim 1$ keV) X-ray emission that exceeds the extrapolation from the power-law continuum observed at higher energies (see, e.g., Turner & Pounds 1989; Masnou et al. 1992). This X-ray “soft excess” has often been interpreted as the high-energy continuation of the UV/EUV/soft X-ray “big blue bump” (BBB), possibly thermal emission from the surface of an accretion disk (cf. Barvainis 1993). Several workers (beginning with Malkan & Sargent 1982) have proposed as an explanation of the Baldwin effect that as QSO luminosity increases, the BBB shifts toward lower energies at higher (OUV) luminosities. As QSOs become more luminous in the optical/UV band, they thereby undergo a weaker increase in l_{x} and, therefore, an increase in α_{ox} . The response of line flux and W_{λ} depends in a fairly complicated manner on the peak energy of the BBB, on the BBB normalization relative to the power-law continuum, and on the ionization and heating continuum of

the line species in question. Detailed photoionization modeling using a variety of input continua, impinging on an ensemble of clouds from the broad- to the narrow-line region, including full self-shielding and optical depth effects, is called for (see, e.g., Korista et al. 1997a; Baldwin et al. 1995; Shields, Ferland, & Peterson 1995). On average, the strongest effect may be that higher luminosity QSOs may undergo spectral evolution such that fewer photons from a soft X-ray excess/BBB component are available for ionization.

A shift of the BBB to lower energies at higher luminosity implies that the soft X-ray excess should decrease to higher luminosities. An apparent hardening of the soft X-ray PL spectral index has been seen in composite *ROSAT* spectra of LBQS QSOs toward higher redshifts (see, e.g., Schartel et al. 1996) that gibes with this picture, but again, higher energy rest frame X-ray emission is observed in most high-luminosity objects, for which a higher intrinsic column is required before absorption can be detected. In this picture, a stronger BEff might be expected for species of higher ionization energy. There is some evidence for such a trend (Zheng, Fang, & Binette 1992). The intrinsic SED model does not predict absorption features but does imply that the α_{ox} (l_{opt}) relation should persist even in soft X-ray selected samples.

6. SUMMARY

By contrasting the composite optical/UV spectra of large samples of X-ray bright and X-ray faint QSOs, we have unveiled significant new correlations with X-ray brightness as characterized by α_{ox} . We find that [O III] emission is at least 2.5 times stronger in our XB sample. Proper subtraction of Fe II suggests a true ratio closer to 5. We find that other, much weaker narrow optical forbidden lines ([O II] and [Ne V]) are enhanced by factors of 2 to 3 in our composites. Narrow-line emission is also strongly enhanced in the XB UV composite. Broad permitted line fluxes are slightly larger for both XB composites, but velocity widths in the broad emission-line region are not significantly affected. The narrow/broad line ratio stays similar or increases with X-ray brightness for all strong lines *except* H β .

We also find that UV Fe II and optical Fe II emission are correlated in opposite senses with α_{ox} . Optical Fe II equivalent widths decrease with X-ray brightness, while UV iron equivalent widths increase. This confirms similar suggestions elsewhere (see, e.g., Green et al. 1995; Lipari 1994; Boroson & Meyers 1992). Proper modeling of nonradiative heating, optical depth effects, and iron recombination rates, along with improved methods of Fe II emission measurements, may all be needed to contribute to the solution of this intriguing observation.

Broad emission lines differ less between XB and XF QSOs than do narrow lines. Our interpretation of the data is that absorbers tend to obscure the line of sight to the central ionizing source both from us and from the NLR. A similar conclusion indicating that less altered continuum radiation reaches the BLR was recently suggested from different lines of evidence by Korista, Ferland, & Baldwin (1997b).

Our tests on complementary subsamples indicate that spectral differences between subsamples divided by α_{ox} exceed those seen between samples divided by luminosity or radio loudness. In particular, we propose that the Baldwin

effect may be a secondary correlation to the primary relationship between α_{ox} and emission line equivalent width. One test of this is that the Baldwin effect should be dominated by narrow-line components.

We note that for 23 UV-excess selected (PG) QSOs observed in the *ROSAT* bandpass (Laor et al. 1997), correlations of emission line parameters (FWHM [H β] and optical Fe II and [O III] strengths) are clearly stronger with α_{X} than with α_{ox} . However, a correlation exists between α_{ox} and α_{X} ; X-ray bright QSOs (with small α_{ox}) tend to have flat (hard) α_{X} . At these and slightly lower luminosities (Seyfert 1 galaxies; see, e.g., Boller, Brandt, & Fink 1996), only objects with flat (hard) α_{X} have large FWHM (H β). If H β is representative, the combination of these two trends would predict that XB QSOs should on average have broader emission lines, counter to the overall trends seen in our samples. Of the emission lines to which we can fit two components (Ly α , C IV, Mg II, and H β), it is the *only* line for which the percentage of total line flux in the narrow-line component may be *larger* in the XF composite. Since H β appears to be unique among the larger variety of emission lines studied here, it is clear that H β may not be the best or only representative of BLR line widths. Fitting the H β line in our optical composites with a *single* Gaussian component leads to conclusions similar to those of these previous studies (i.e., that FWHM [H β] is larger in the XF composite). However, fitting narrow- and broad-line components separately reveals that H β has a stronger broad component in the XB composite and a larger broad/narrow line ratio, while the actual FWHM is similar to that in the XF composite. This reveals that single Gaussian fits to compound lines must be interpreted with caution. Furthermore, we also caution that the luminosity ranges for these (PG and LBQS) samples are disjoint. However, since α_{X} and not α_{ox} seems to have the more fundamental correlation with both H β and [O III] in Laor et al. (1997), we highlight the need for correlation of α_{X} with a wider range of emission line measurements.

The parameters emphasized here, α_{ox} and narrow-line emission, also appear to be linked to the following quantities: X-ray spectral slope α_{X} , Fe II strength, luminosity, radio loudness (see, e.g., Laor et al. 1997; Lawrence et al. 1997; Green et al. 1995; BG92). We suggest here that the as yet mysterious physical link between these diverse properties is intimately related to high-velocity outflowing winds near the nucleus that, by absorbing the intrinsic nuclear continuum, strongly affect the radiation observed at larger distances. The continuum impinging on the NLR is closest to that received by distant observers like ourselves but is quite different from that arriving at the BLR. Material in the BLR itself may reprocess the intrinsic continuum issuing from the unshrouded QSO nucleus.

Only some of the correlations between measured line and continuum parameters are intrinsic, and others simply add dispersion to more primary correlations. The principal physical processes must be extracted from the principle observational eigenvectors in a multivariate, multi-wavelength approach, with careful attention to continuum slopes and detailed emission line fits. We are accumulating a high-quality homogeneous database including all this information for a large sample of QSOs, primarily from the *ROSAT* and *HST* archives. We believe that multi-wavelength studies such as this show promise for significant advances in our understanding.

Thanks to Marianne Vestergaard for performing the iron subtraction, to Craig Foltz for the LBQS spectra, to Ken Lanzetta for the *IUE* QSO atlas, and to Todd Boroson for the optical Fe II template. The author gratefully acknowledges support provided by NASA through grant NAG5-1253 and contract NAS 8-39073 (ASC), as well as HF-1032.01-92A awarded by the Space Telescope Science

Institute, which is operated by the Association of Universities for Research in Astronomy, Inc., under NASA contract NAS 5-26555. This research has made use of the NASA/IPAC Extragalactic Database (NED) which is operated by the Jet Propulsion Laboratory, California Institute of Technology, under contract with the National Aeronautics and Space Administration.

REFERENCES

- Baldwin, J. A. 1977, *ApJ*, 214, 679
 Baldwin, J. A., Ferland, G., Korista, K., & Verner, D. 1995, *ApJ*, 455, 119
 Barvainis, R. 1993, *ApJ*, 412, 513
 Boller, T., Brandt, W. N., & Fink, H. 1996, *A&A*, 305, 53
 Boroson, T. A., & Green, R. F. 1992, *ApJS*, 80, 109
 Boroson, T. A., & Meyers, K. A. 1992, *ApJ*, 397, 442
 Brandt, W. N., Mathur, S., & Elvis, M. 1997, *MNRAS*, 285, 25P
 Cristiani, S., & Vio, R. 1990, *A&A*, 227, 385
 Falcke, H., Sherwood, W., & Patnaik, A. R. 1996, *ApJ*, 471, 106
 Ferland, G. F., & Shields, G. A. 1985, in *Astrophysics of Active Galaxies and Quasi-stellar Objects*, ed. J. Miller (Mill Valley: University Science), 157
 Francis, P. J., Hewett, P., Foltz, C., Chaffee, F., Weymann, R. J., & Morris, S. 1991, *ApJ*, 373, 465
 Francis, P. J., Hooper, E. J., & Impey, C. D. 1993, *AJ*, 106, 417
 Green, P. J. 1996, *ApJ*, 467, 61
 Green, P. J., Aldcroft, T., Mathur, S., & Schartel, N. 1997, *ApJ*, 484, 135
 Green, P. J., & Mathur, S. 1996, *ApJ*, 462, 637
 Green, P. J., et al. 1995, *ApJ*, 450, 51
 Grossan, B. A. 1992, Ph.D. thesis, MIT
 Hamann, F., Barlow, T. A., Cohen, R. D., Junkkarinen, V. T., & Burbidge, E. M. 1997, in *ASP Conf. Proc. 128, Mass Ejection from Active Galactic Nuclei*, ed. N. Arav, I. Shlosman, & R. Weymann (San Francisco: ASP), 19
 Hewett, P. C., Foltz, C. B., & Chaffee, F. H. 1995, *AJ*, 109, 1498
 Irwin, M. J., & Trimble, V. 1984, *AJ*, 89, 93
 Korista, K., Baldwin, J. A., Ferland, G., & Verner, D. 1997a, *ApJS*, 108, 401
 Korista, K., Ferland, G., & Baldwin, J. A. 1997b, *ApJ*, 487, 555
 Kriss, G. 1994, in *ASP Conf. Proc. 61, Astronomical Data Analysis Software and Systems III*, ed. D. R. Crabtree, R. J. Hanisch, & J. Barnes (San Francisco: ASP), 437
 Krolik, J. H., & Kallman, T. R. 1988, *ApJ*, 324, 714
 La Franca, F., Franceschini, A., Cristiani, S., & Vio, R. 1995, *A&A*, 299, 19
 Laor, A., Fiore, F., Elvis, M., Wilkes, B. J., & McDowell, J. C. 1997, *ApJ*, 477, 93
 Lawrence, A., Elvis, M., Wilkes, B. J., McHardy, I., & Brandt, N. 1997, *MNRAS*, 285, 879
 Lipari, S. 1994, *ApJ*, 436, L102
 Malkan, M. A., & Sargent, W. L. W. 1982, *ApJ*, 254, 22
 Masnou, J.-L., Wilkes, B. J., Elvis, M., Arnaud, K. A., & McDowell, J. C. 1992, *A&A*, 253, 35
 Mathur, S. 1994, *ApJ*, 431, L75
 Mathur, S., Elvis, M., & Wilkes, B. J. 1995, *ApJ*, 452, 230
 Osmer, P. S., Porter, A. C., & Green, R. F. 1994, *ApJ*, 436, 678
 Reynolds, C. S. 1997, *MNRAS*, 286, 513
 Schartel, N., et al. 1996, *MNRAS*, 283, 1015
 Shields, J. C., Ferland, G. J., & Peterson, B. M. 1995, *ApJ*, 441, 507
 Turner, T. J., & Pounds, K. A. 1989, *MNRAS*, 240, 833
 Tytler, D., & Fan, X.-M. 1992, *ApJS*, 79, 1
 Veron-Cetty, M.-P., & Veron, P. 1996, *ESO Sci. Rep.*, 17, 1
 Vestergaard, M., & Green, P. J. 1998, in preparation
 Wang, T., Brinkmann, W., & Bergeron, J. 1996, *A&A*, 309, 81
 Wilkes, B. J., Tananbaum, H., Worrall, D. M., Avni, Y., Oey, M. S., & Flanagan, J. 1994, *ApJS*, 92, 53
 Wills, B. J., & Brotherton, M. S. 1995, *ApJ*, 448, 81
 Zamorani, G., Marano, B., Mignoli, M., Zitelli, V., & Boyle, B. J. 1992, *MNRAS*, 256, 238
 Zheng, W., Fang, L. Z., & Binette, L. 1992, *ApJ*, 392, 74
 Zheng, W., Kriss, G. A., & Davidsen, A. F. 1995, *ApJ*, 440, 606
 Zheng, W., Kriss, G. A., Telfer, R. C., Grimes, J. P., & Davidsen, A. F. 1996, *ApJ*, 475, 469
 Zheng, W., & Malkan, M. A. 1993, *ApJ*, 415, 517